BNL-111943-2016-JA

THE MIDLATITUDE CONTINENTAL CONVECTIVE CLOUDS EXPERIMENT (MC3E)

BY M. P. JENSEN, W. A. PETERSEN, A. BANSEMER, N. BHARADWAJ, L. D. CAREY, D. J. CECIL, S. M. COLLIS, A. D. DEL GENIO, B. DOLAN, J. GERLACH, S. E. GIANGRANDE, A. HEYMSFIELD, G. HEYMSFIELD, P. KOLLIAS, T. J. LANG, S. W. NESBITT, A. NEUMANN, M. POELLOT, S. A. RUTLEDGE, M. SCHWALLER, A. TOKAY, C. R. WILLIAMS, D. B. WOLFF, S. XIE, AND E. J. ZIPSER

MC3E is a field campaign aimed at acquiring a more complete understanding of the physical processes driving the life cycle of midlatitude convective clouds.

Convective clouds play a critical role in Earth's climate system. Convective processes redistribute water, heat, and momentum through the depth of the troposphere. These cloud systems act as a sink of total water in the atmospheric column, contribute to the local energy balance through diabatic heating effects, and feed back onto the local environment by impacting the subsequent formation of clouds. Continental convective clouds, through their precipitation processes, further impact ecosystems and water resource management and contribute to catastrophic weather events including severe weather and flooding. From an observational perspective, it is important to accurately detect, monitor, and

AFFILIATIONS: JENSEN AND GIANGRANDE—Brookhaven National Laboratory, Upton, New York; PETERSEN, GERLACH, AND WOLFF—NASA Goddard Space Flight Center, Greenbelt, Maryland, and NASA Wallops Flight Facility, Wallops Island, Virginia; BANSEMER AND A. HEYMSFIELD—National Center for Atmospheric Research, Boulder, Colorado; BHARADWAJ—Pacific Northwest National Laboratory, Richland, Washington; CAREY—University of Alabama in Huntsville, Huntsville, Alabama; CECIL AND LANG—NASA Marshall Space Flight Center, Huntsville, Alabama; COLLIS—Argonne National Laboratory, Argonne, Illinois; DEL GENIO—NASA Goddard Institute for Space Studies, New York, New York; DOLAN AND RUTLEDGE—Colorado State University, Fort Collins, Colorado; G. HEYMSFIELD AND SCHWALLER—NASA Goddard Space Flight Center, Greenbelt, Maryland; KOLLIAS—McGill University, Montreal, Quebec, Canada; NESBITT—University of Illinois at Urbana–Champaign, Urbana, Illinois; NEUMANN AND POELLOT—University of North Dakota, Grand Forks, North Dakota; TOKAY—University of Maryland, Baltimore County, Baltimore, and NASA Goddard Space Flight Center, Greenbelt, Maryland; WILLIAMS—University of Colorado, Boulder, Boulder, Colorado; XIE—Lawrence Livermore National Laboratory, Livermore, California; ZIPSER—University of Utah, Salt Lake City, Utah
CORRESPONDING AUTHOR: Michael P. Jensen, Brookhaven National Laboratory, P.O. Box 5000, MS 490D, Upton, NY 11973
E-mail: mjensen@bnl.gov

The abstract for this article can be found in this issue, following the table of contents.
DOI:10.1175/BAMS-D-14-00228.1

In final form 12 November 2015

estimate convective precipitation over continental-scale domains using satellite- and/or ground-based remote sensing. It is equally important to improve the representation of the physics of convective clouds in numerical models. The latter remains one of the most challenging issues in operational weather and global climate modeling (Klein and Del Genio 2006) because of the wide assortment of spatial and temporal ranges over which dynamical, microphysical, and radiative processes act. For these reasons, it is important to improve our understanding of convective processes through greater accuracy in measurements, particularly precipitation, and to utilize this to improve their representation in models.

To address these critical needs, the U.S. Department of Energy (DOE) Atmospheric Radiation Measurement (ARM; Mather and Voyles 2013; Ackerman and Stokes 2003; Stokes and Schwartz 1994) Program and the National Aeronautics and Space Administration's (NASA) Global Precipitation Measurement (GPM; Hou et al. 2014) mission collaborated to jointly lead the Midlatitude Continental Convective Clouds Experiment (MC3E; Jensen et al. 2010; Petersen and Jensen 2012). MC3E took place from 22 April through 6 June 2011, and was focused at and around the DOE ARM Southern Great Plains (SGP) Central Facility (CF) (www.arm.gov/sites/sgp) in north-central Oklahoma, where an extensive array of both airborne and ground-based instrumentation (Fig. 1) was deployed. The campaign leveraged the largest ground-based observing infrastructure available in the central United States, including recent upgrades through the American Recovery and Reinvestment Act of 2009 (Mather and Voyles 2013), combined with an extensive sounding array, remote sensing and in situ aircraft observations, and additional radar and in situ precipitation instrumentation. The MC3E science objectives were motivated by the need to acquire a more complete understanding of the complex and interconnected physical processes driving the life cycle of midlatitude convective clouds and the characteristics of its precipitation.

Specifically, the two primary MC3E objectives were to collect observations to 1) advance our understanding of different components of convective simulations and microphysical parameterizations and 2) improve the fidelity of space-based estimates of rainfall over land. These complementary objectives required specific science-driven targets that could only be accomplished with a multiplatform coordinated strategy. In particular, these targets included 1) a definition of the vertical and horizontal structure of the atmospheric thermodynamic state and its evolution to form a basis for the construction of accurate large-scale forcing environments for cloud and land surface model simulations, 2) characterization of the variability of cloud and precipitation microphysical properties through the convective cloud life cycle from surface- and aircraft-based remote sensing and in situ observations, and 3) identification of updraft and downdraft dynamics within convective clouds and their relation to lower-tropospheric stability and boundary layer structure.

FIELD EXPERIMENT STRATEGY AND OPERATIONAL NETWORKS. The MC3E observing strategy focused on connecting data from three different vantage points (Fig. 2). The "signal" measured by downward-viewing remote sensing observations of convection was provided by high-altitude airborne platforms carrying instruments similar to those flying on the GPM *Core Observatory*. These data were combined with the in situ cloud properties observed by cloud-penetrating aircraft. Finally, measurements of precipitation on the ground extending back upward through hydrometeors of all kinds in the convective cloud column were obtained via combined use of ground-based radars and supporting ground instrumentation.

Aircraft platforms and instrumentation. At the top of the sampling domain (~20 km in altitude), the NASA ER-2 aircraft functioned as a GPM core-satellite sampling simulator. It carried the dual-frequency, dual-beam (30° and 40° incidence angles), nadir-pointing Doppler, High-Altitude Imaging Wind and Rain Airborne Profiler (HIWRAP; Heymsfield et al. 2013), and two multifrequency passive microwave radiometers: the Advanced Microwave Precipitation Radiometer (AMPR; Spencer et al. 1994) and the Conical Scanning Microwave Imaging Radiometer (CoSMIR) (Table 1; Wang et al. 2007). The University of North Dakota (UND) Cessna Citation II jet aircraft served as the in situ microphysics platform with a primary emphasis placed on the measurements of ice-phase hydrometeors at altitudes between the melting level and cloud top (~4–13 km). The Citation carried a standard suite of meteorological instruments together with cloud and precipitation microphysical probes and total and liquid water content probes (Table 2). Independent of, but in coordination with the MC3E campaign, the NASA Marshall Space Flight Center Marshall Airborne Polarimetric Imaging Radiometer (MAPIR) instrument flew several test flights toward the end of the experiment, making soil moisture measurements using its L-band radiometer. A summary

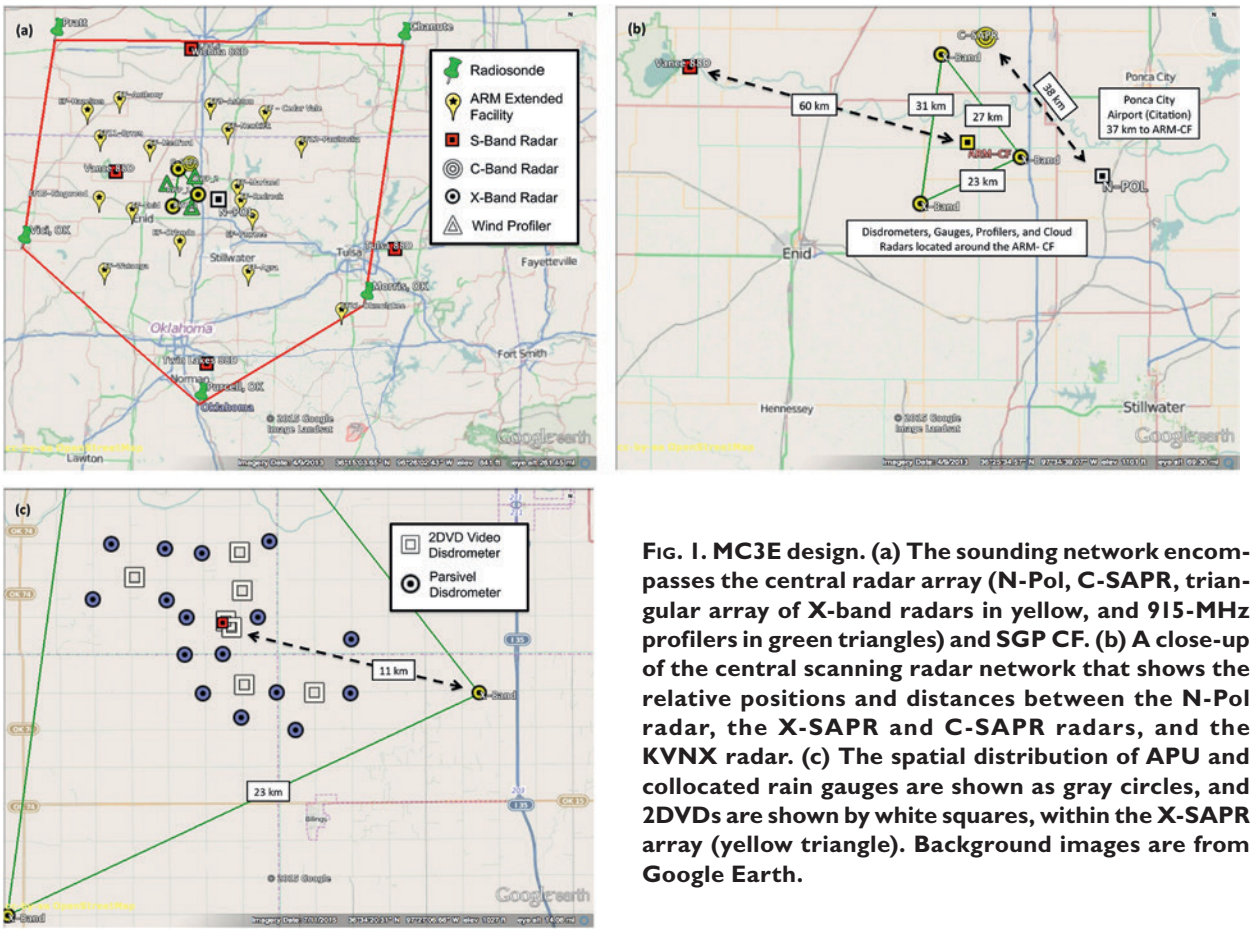

Fig. 1. MC3E design. (a) The sounding network encompasses the central radar array (N-Pol, C-SAPR, triangular array of X-band radars in yellow, and 915-MHz profilers in green triangles) and SGP CF. (b) A close-up of the central scanning radar network that shows the relative positions and distances between the N-Pol radar, the X-SAPR and C-SAPR radars, and the KVNX radar. (c) The spatial distribution of APU and collocated rain gauges are shown as gray circles, and 2DVDs are shown by white squares, within the X-SAPR array (yellow triangle). Background images are from Google Earth.

of the aircraft flight hours is provided in Table 3. The ER-2 flew a total of 14 science flights totaling more than 73 flight hours from Offutt Air Force Base in Bellevue, Nebraska, while the Citation based at Ponca City, Oklahoma, flew 15 data missions totaling 42.6 flight hours. Five missions were performed with coordinated ER-2 above-cloud remote sensing observations and UND Citation in situ observations within 100 km of the CF.

Sounding network. At the largest scale (90,000 km^2; Fig. 1a), a radiosonde network was deployed (Jensen et al. 2015) to quantify the temperature, humidity, and wind properties of the environment surrounding the ARM SGP CF. MC3E staff launched 1,348 coordinated weather balloons from six sites at a frequency of four times per day under nonconvective conditions in order to partially sample the diurnal cycle. On days for which convective conditions were forecast and aircraft operations were planned, sounding operations switched to a high-frequency launch schedule of eight times per day. All sounding sites used Vaisala model RS92-SGP radiosondes attached to a 350-g helium-filled meteorological balloon.

Radar network. MC3E included a multiscale, multiparameter radar array located within 60 km of the ARM SGP CF. These radars were under the umbrella of the Vance Air Force Base (AFB), Oklahoma (KVNX), operational Weather Surveillance Radar-1988 Doppler (WSR-88D) and nested inside the radiosonde network (Fig. 1b). MC3E scanning radar deployments included the NASA S-band dual-polarization Doppler radar (N-Pol), the NASA dual-frequency, dual-polarized Doppler radar (D3R), and the dual-polarization X- and C-band Scanning ARM Precipitation Radars (X-SAPR and C-SAPR, respectively). Four ARM wind profilers, deployed in the dual-Doppler lobes of the ARM radar network, supported the scanning radars. Two additional National Oceanic and Atmospheric Administration (NOAA) profiling radars were placed at the SGP CF to complement the Ka-band ARM zenith radar (KAZR) and the Ka–W-band scanning ARM cloud radar (SACR) system. Details and the nominal role for each radar are summarized in Table 4.

Disdrometer network. Surrounding the SGP CF was a dense network of 18 autonomous Particle Size and

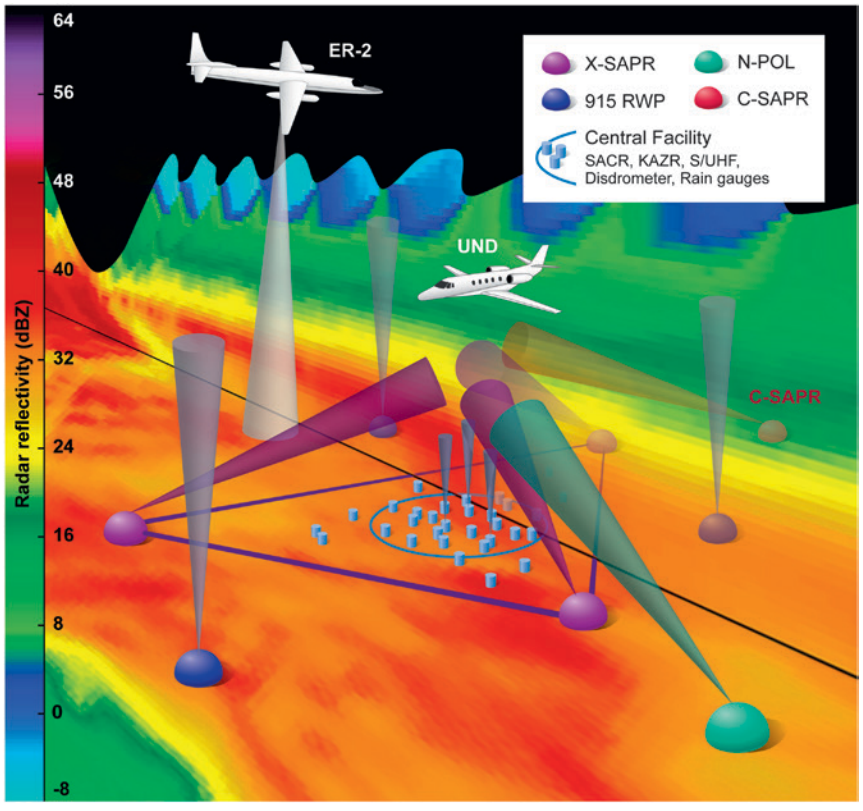

Fig. 2. Conceptual 3D sampling strategy for MC3E. Sampling from aircraft (ER-2 and UND Citation aircraft) occurred over a nested multifrequency ground-based network of radars (X-SAPR, C-SAPR, N-Pol, SACR, KAZR, S band/UHF, and 915-MHz profilers), covering a dense array of disdrometers and rain gauges. Radar data slices are made using the Python–ARM Radar Toolkit (Heistermann et al. 2015).

Velocity (PARSIVEL) disdrometers [Autonomous Parsivel Units (APUs); Thurai et al. 2011; Tokay et al. 2013], 16 rain gauge pairs, and seven 2D video disdrometers (2DVDs; Schönhuber et al. 2008) (Fig. 1c). These instruments were deployed within a 6-km radius of the CF. The APUs and rain gauges measured rainfall and drop size distribution (DSD) correlation properties at kilometer scales. The 2DVDs provided a DSD reference measurement to the APU network and the results were used to calibrate dual-polarimetric radar measurements and DSD retrievals. Previous work (Tokay et al. 2013) has shown that the third-generation 2DVDs deployed during MC3E have smaller wind-induced biases and show good agreement with rain gauge–measured total rainfall.

ARM SGP facility. At the time of the MC3E campaign, the SGP facility consisted of the CF (36.695°N, 97.485°W) and 20 extended facilities covering an area of approximately 150 km × 150 km. The extended facilities include instrumentation aimed at quantifying the spatial variability of surface heat, moisture, and momentum fluxes across the SGP region (www.arm.gov/sites/sgp/E). At the SGP CF there is a comprehensive instrumentation suite for cloud, precipitation, aerosols, and atmospheric-state observations (www.arm.gov/sites/sgp/C). Most important for the goals of MC3E are remote sensing observations from a Raman lidar, a two-channel microwave radiometer, and the Atmospheric Emitted Radiance Interferometer (AERI) that are used to retrieve atmospheric water vapor. A micropulse lidar, ceilometer, and total-sky imager (TSI; Long et al. 2001) provide complementary information on cloud properties. The Advanced Microwave Radiometer for Rain Identification (ADMIRARI; Saavedra et al. 2011) operated at the ARM CF site with its 19- and 37-GHz passive microwave radiometers and a K-band Micro Rain Radar to detect and separate contributions to cloud total water content from cloud and rainwater components.

OVERVIEW OF LARGE-SCALE WEATHER CONDITIONS. Xie et al. (2014) used the constrained variational analysis approach of Zhang and Lin (1997) in order to derive the large-scale forcing conditions over the MC3E domain. This dataset is used to summarize the large-scale weather conditions during the campaign in Fig. 3. The first few days of the campaign (22–28 April) were dominated by high values of low-level moisture (Fig. 3a), some periods of moderate CAPE (Fig. 3c), and low rain rates resulting from some widespread shallow, stratiform rain events. This was followed by nearly two weeks of dry conditions, no precipitation, and little CAPE. Low-level moisture returned by 10 May along with one period of high CAPE (8–12 May), which brought some significant precipitation on 11 May and a second period of high CAPE after 19 May that resulted in some more significant precipitation events. In the days that followed this deep-convective pattern (not

Table 1. ER-2 instruments (H indicates horizontal and V indicates vertical).	
Instrument	**Characteristics**
AMPR	Passive microwave radiometer
Frequencies	10.7, 19.35, 37.1, and 85.5 GHz; all channels; H/V
Resolution at 20-km range	0.6 km (85.5 GHz),1.5 km (37.1 GHz), and 2.8 km (10.7–19.35 GHz)
CoSMIR (radiometer, H + V)	Passive microwave radiometer
Frequencies	52, 89 (H/V), 165.5 (H/V), 183.3 ± 1, 183.3 ± 3, and 183.3 ± 8 GHz
Resolution at 20-km range	1.4-km footprint at nadir
HIWRAP radar	
Frequencies	13.91/13.35 GHz, 35.56/33.72 GHz
Transmit peak power	30 W (Ku), 10 W (Ka)
3-dB beamwidth (resolution at 20-km range)	2.9° (1.02 km) Ku, 1.2° (0.36 km) Ka
Min reflectivity at 75-m resolution, 20-ms chirp, 10 km	0.0, –5.0 dBZe

shown), significant precipitation was not recorded over campaign facilities. The MC3E campaign collected a rich dataset from a wide variety of cloud and precipitation conditions. Campaign conditions included shallow boundary layer clouds, nocturnal elevated convection, and deep, organized convective storms (Table 5).

EXAMPLES OF OBSERVED CONVECTIVE SYSTEMS. This section highlights three deep convective events captured during this campaign. The 11 May event had a very large amount of CAPE (Fig. 3c) near the beginning of a period where the lower atmosphere was entering a moistening trend but still had a midlevel humidity deficit (Fig. 3a). The 20 May event, which produced extensive cloudiness at all levels, occurred in a very humid environment through the depth of the troposphere (Fig. 3a). The 23 May event occurred during a period with a rather dry troposphere above the boundary layer (Fig. 3a) with relatively large CAPE (but not as large as on 11 May) and produced much less cloudiness compared to 20 May.

Table 2. Citation instruments.		
Instrument	**Measurement**	**Range**
Cloud imaging probe (CIP)	Cloud and precipitation particle spectra	0.025–1.5 mm
2D cloud imaging probe (2D-C)	Cloud and precipitation particle spectra	0.03–1.0 mm
High-volume precipitation spectrometer, version 3 (HVPS-3)	Precipitation particle spectra	0.15–19.2 mm
Cloud particle imager (CPI)	Cloud particle images	0.002–2.3 mm
Cloud droplet probe (CDP)	Cloud droplet spectra	2–50 μm
King hot-wire liquid water content (LWC) probe	Cloud liquid water	0.01–5 g m^{-3}
Nevzorov probe	Total water content	0.03–3 g m^{-3}
Rosemount icing probe	Supercooled liquid water	Supercooled water detection
Condensation particle counter	Aerosol–condensation nuclei	10-nm cut
Ultrahigh sensitivity aerosol spectrometer (UHSAS)	Aerosol	0.06–1 μm
Temp probe	Ambient air temperature	—
Static pressure sensor	Ambient air pressure	—
Chilled-mirror dewpoint hygrometer	Water vapor content	—
Tunable diode laser hygrometer	Water vapor content	—

Table 3. Summary of aircraft flights.	
Airborne case type	**Dates**
Coordinated ER-2 and Citation within 100 km of CF	25 Apr, 11 May, 18 May, 20 May, 23 May
ER-2 and Citation outside CF coverage (northeast KS)	1 Jun
Citation-only precipitating cloud missions	27 Apr, 1 May, 10 May, 24 May
Citation-only nonprecipitating cloud missions	27 May, 2 Jun
ER-2 land surface	25 Apr, 8 May, 29 May

11 May 2011 mesoscale convective system. Early in the day, a surface cold front propagated across the Texas–Oklahoma Panhandle region (Fig. 4), initiating organized severe convection. A mesoscale convective system (MCS) organized with a parallel stratiform precipitation region north of the main convective band around 1600 UTC while the storm motion was to the northeast. Figure 4 (bottom) shows a plan position indicator (PPI) of radar reflectivity from the KVNX radar at 1755 UTC, just before the system reached the ARM CF, as viewed during operations using the Real Time Mission Monitor (RTMM; Blakeslee et al. 2007). The MCS transitioned into a trailing stratiform mode between 1800 and 1900 UTC as it passed over the CF. In this section, we focus on in situ precipitation microphysics observations from the Citation and the remote sensing NOAA wind profiler during this event.

Two hours of stacked aircraft transects were collected prior to the ER-2 recall because of impending

Table 4. Summary of MC3E radar assets.				
Radar	**Frequency**	**Scanning strategy**	**Primary observational objective**	**Reference**
NASA S-band dual-polarization Doppler radar (N-Pol)	2.7–2.9 GHz	Targeted RHI scanning and select sectored PPIs	Precipitation microphysics	Gerlach and Petersen 2011
Three X-band Scanning ARM Precipitation Radars (X-SAPR)	9.35–9.45 GHz	Multitilt PPI volume coverage patterns	Multi-Doppler wind retrievals	Mather and Voyles 2013
C-band Scanning ARM Precipitation Radar (C-SAPR)	6.25 GHz	Multitilt PPI volume coverage patterns and select targeted RHIs	Large-scale volumetric precipitation mapping	
NOAA S-band profiling radar	3 GHz	Vertically pointing	Vertical air motions and precipitation microphysics	Williams 2012
NOAA wind profiler	449 MHz	Vertically pointing	Vertical air motion and precipitation microphysics	
Four ARM radar wind profilers	915 MHz	Vertically pointing	Vertical air velocity and precipitation microphysics	Giangrande et al. 2013b; Tridon et al. 2013
Dual-frequency Ka–Ku-band, dual-polarized Doppler radar (D3R)	35.5 and 13.9 GHz	Multitilt PPI and vertically pointing operations	Precipitation microphysics	Vega et al. 2010, 2014
Ka-band ARM zenith radar (KAZR)	35 GHz	Vertically pointing	Cloud properties	Kollias et al. 2007
Ka–W-band scanning ARM cloud radar (Ka–W SACR)	35 and 94 GHz	Horizon-to-horizon RHI, crosswind sectors, along-wind RHI, vertically pointing	Cloud properties	Kollias et al. 2014a,b

weather conditions at Offutt AFB. The Citation was positioned for an additional 1.5 hours to further sample weaker stratiform conditions coordinated with ground facilities. At the top altitude of the Citation stack (7.5 km MSL, –25°C), the stratiform region was supersaturated with respect to ice. Optical array probe imagery showed large (>1-cm diameter) ice aggregates mixed with smaller ice particles at this level (Fig. 5). Below 7.5 km MSL, humidity values were lower and less uniform, with some areas having a relative humidity less than 80% with respect to ice. In general, the microphysical properties of this system were similar to the properties of trailing stratiform regions observed in other studies (e.g., Houze 2014 and references therein) with particle size increasing downward and aggregation noted at lower altitudes.

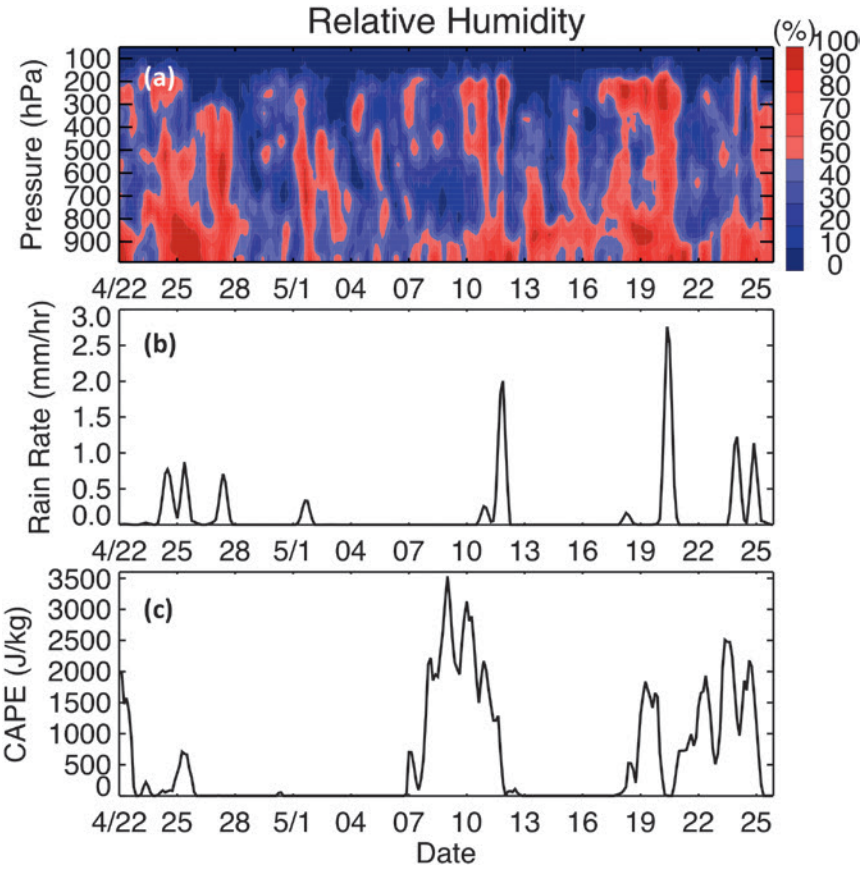

Fig. 3. Large-scale meteorological conditions. Time series derived from the 150-km ARM large-scale forcing dataset including the (a) profile of domain-averaged RH, (b) domain-averaged rain rate, and (c) CAPE.

Several radar observations complemented the aircraft observations, including the NOAA wind profilers. Figure 6 shows profiles of reflectivity-weighted Doppler velocity spectra during stratiform rain on 11 May (Figs. 6a,b,d,e). The S-band Doppler velocity spectra files (Figs. 6b,e) were sensitive only to

Table 5. Summary of MC3E cases.

Category	Description	No. of days sampled	Dates
1	Convective line/cell events	8	22 and 25 Apr
			11, 18, 20, 23, 24, and 31 May
2	Widespread stratiform rain	3	27 Apr
			1 and 10 May
3	Elevated weak (overnight) rain	3	23 and 24 Apr
			18 May
4	Boundary layer clouds	10	26 Apr
			5, 13, 14, 15, 19, 27, 28, and 29 May
			1 Jun
5	Mid- or upper-level clouds	7	2, 3, 8, 9, 25, and 26 May
			2 Jun
6	Clear	14	Remaining days

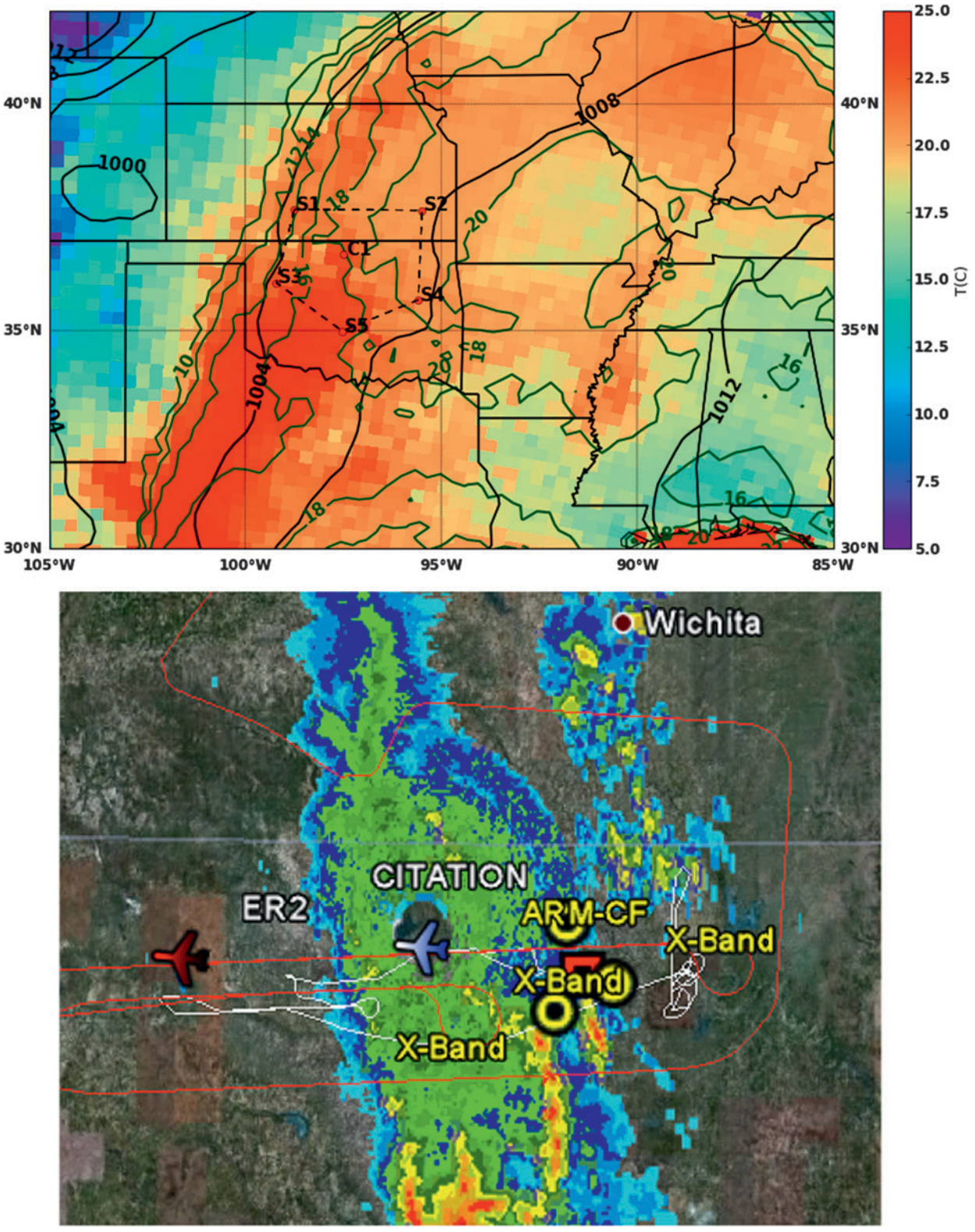

Fig. 4. (top) The 1200 UTC 11 May 2011 surface meteorological analysis based on National Centers for Environmental Prediction (NCEP) North American Regional Reanalysis (NARR) output showing the surface pressure (hPa; contours) and surface temperature (colors). The MC3E sounding array hexagon is indicated by the dashed lines. (bottom) RTMM image during MC3E field operations showing a PPI of radar reflectivity from the KVNX radar at 1755 UTC with flight positions of ER-2 (red line) and Citation (white line) overlaid in the observational network.

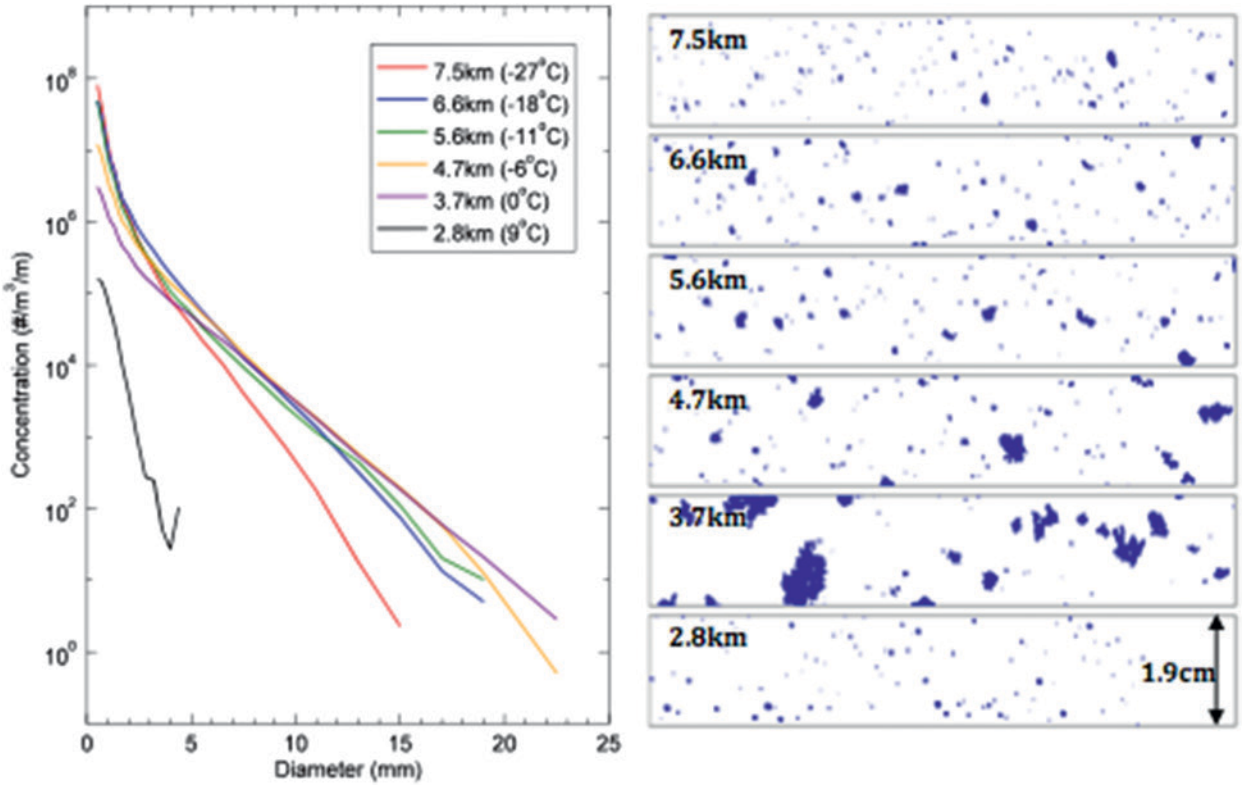

Fig. 5. Examples of (left) PSDs and (right) images from the HVPS-3 with the mean height (km MSL) and temperature of the corresponding leg in order of descending height on 11 May.

hydrometeor motion (Rayleigh scattering returns, drop fall speeds plus ambient air motion), while the 449-MHz profiler (Figs. 6a,d) was sensitive to both the ambient air motion (Bragg scattering returns from changes in the atmospheric refractive index caused by turbulence and humidity gradients) and the hydrometeor returns, as also sampled by the S-band radar. The air motion signal, if detected by the 449-MHz profiler, is much weaker than the hydrometeor motion signal and will produce a second peak in the 449-MHz profiler spectra. To help isolate this weaker ambient air motion Bragg scattering peak in the 449-MHz profiler spectra, a dual-frequency retrieval technique used the S-band spectra to suppress the hydrometeor motion signal in the 449-MHz spectra (Williams 2012). The two profile times in Fig. 6 were selected because these hydrometeor profiles contained well-defined radar bright bands near 2.75 km (Figs. 6c,f). These times also had an updraft (Fig. 6a) or downdraft (Fig. 6c) exceeding 2 m s^{-1} near 1.5 km.

These Doppler spectra measurements were used to perform routine column air motion and DSD retrievals for most rain events during MC3E. While details of the air motion and DSD retrievals are provided by Williams (2016), Fig. 7 highlights time–height cross sections of S-band profiler reflectivity (Fig. 7a), profiler-derived mean raindrop diameter D_m (Fig. 7b), and 449/S-band dual-frequency technique air motion retrievals (Fig. 7c) for 11 May. The profiler-derived D_m results show vertical structures that mimic the reflectivity structure (Fig. 7a) more closely than the air motion structure (Fig. 7c). As highlighted with individual spectra profiles (Fig. 6), air motions exceeded 2 m s^{-1} for downdrafts (blue colors) and updrafts (red colors) even while well-defined radar bright bands were near 3 km.

20 May 2011 MCSs. The "golden event" of the MC3E campaign, 20 May, occurred immediately following an extended period of precipitation-free days. Several ingredients came together, including southerly flow at the surface (Fig. 8, top), which provided sufficient low-level moisture return from the Gulf of Mexico. A strong north–south-aligned squall line with substantial trailing stratiform shield formed and propagated across the MC3E domain (Fig. 8, bottom). Coordinated aircraft operations predominantly focused on the sampling of the extended stratiform shield that developed after 1000 UTC over the SGP CF. Multi-Doppler ground facilities also sampled initiating convection and the passage of the squall line over the SGP CF, in addition to the later stratiform conditions.

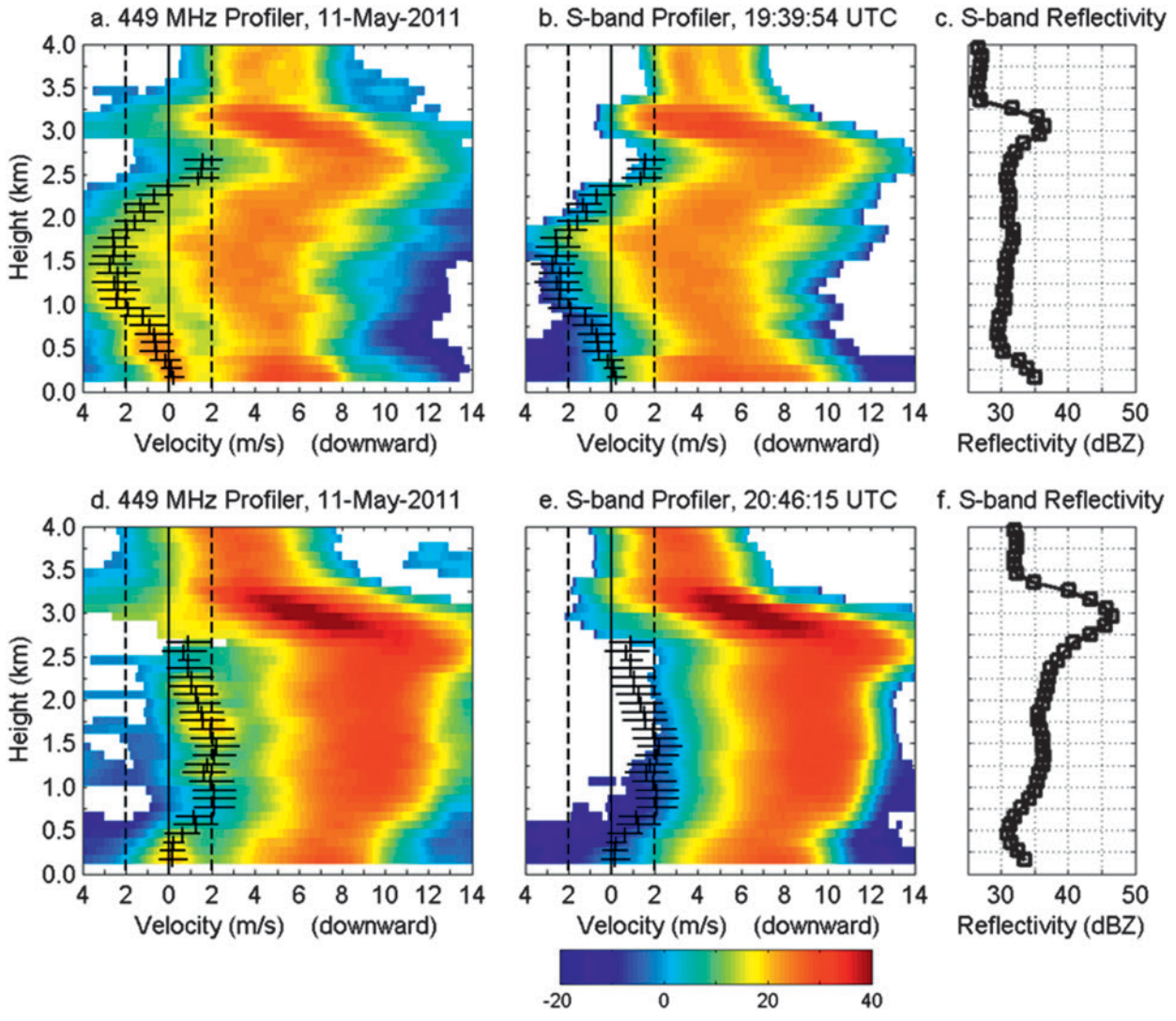

Fig. 6. Vertical profiles of reflectivity-weighted Doppler velocity spectral density during the 11 May 2011 rain event. Near 1940 UTC, (a) 449-MHz profiler spectra, (b) S-band profiler spectra, and (c) S-band profiler reflectivity. Near 2046 UTC, (d) 449-MHz profiler spectra, (e) S-band profiler spectra, and (f) S-band profiler reflectivity. Tick marks indicate retrieved vertical air motion and horizontal lines indicate retrieved air motion peak spectrum width. Colors represent reflectivity spectral density in logarithmic units of 10log[(mm^6 m^{-3})(m s^{-1})$^{-1}$]. While not occurring in all rain event profiles, these two profiles show the precipitation spectra breadth and reflectivity increasing in the lowest 500 m.

There was excellent coordination between the ER-2 and Citation aircraft in stratiform regions (Fig. 8, bottom) for several hours. Here, we highlight these coordinated aircraft observations.

The coordinated ER2 and UND Citation measurements offered the opportunity to examine the assumptions used in radar–radiometer forward models and validate the dual-wavelength retrieval results. Figure 9 shows an example of the trailing stratiform rain with data from HIWRAP, CoSMIR, and the UND Citation in situ aircraft. The ER-2 flew a repeated pattern over the stratiform region, while the Citation descended in altitude underneath the ER-2's flight line, collecting in situ data at temperatures between –20° and –2°C. The HIWRAP reflectivities were lower at Ka band compared to Ku band as a result of non-Rayleigh scattering and attenuation. The microwave brightness temperatures at 165 and 183 GHz were minimized on the right half of the line, indicating larger particle sizes in the ice region. GPM algorithm developers (Olson et al. 2016) are using data such as these for testing the physical assumptions in the satellite retrievals for vertical distributions of hydrometers, mixed phase, etc. The ER-2 data are being used to test to what extent the observed reflectivities at Ku and Ka band agree with the forward-calculated reflectivities obtained using

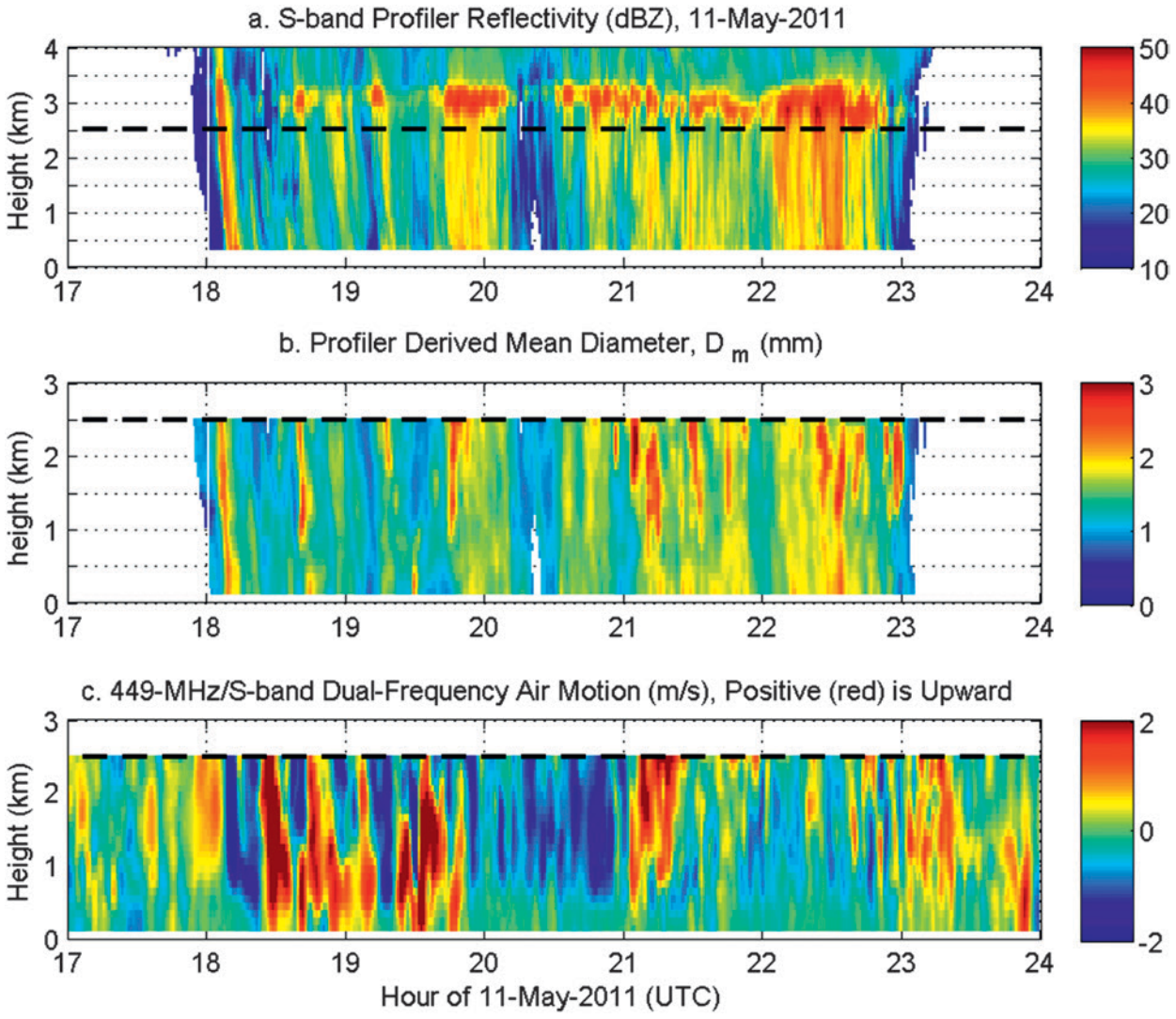

Fig. 7. Vertical structure of precipitation during the 11 May 2011 rain event. (a) The S-band profiler reflectivity from 0.3 to 4 km, (b) profiler-derived mean raindrop diameter, and (c) vertical air motion retrieved from 449-MHz/S-band dual-frequency retrieval method [see Williams (2012) for details]. Dashed line in (a) indicates maximum height of retrievals shown in (b) and (c).

in situ particle size distribution (PSD) and measured ice water content (IWC) observations.

23 May 2011 supercell. A strong dryline advanced over western Oklahoma by early afternoon on 23 May (Fig. 10, top), forcing the development of convection in a southwest–northeast direction by 1930 UTC. Convection propagated eastward into the MC3E target domain by 2200 UTC. The ER-2 overflew the intense developing convective line to the west of the CF, while the Citation sampled the fresh anvils to the south of the CF. Cells rapidly produced anvils that expanded to the east-southeast. These became the primary target for aircraft operations over the next several flight hours (Fig. 10, bottom). Several passes of the Citation and ER-2 were coordinated along N-Pol and C-SAPR range–height indicator (RHI) lines. Here, we highlight the scanning precipitation radar observations in comparison with the Citation observations.

The extensive ground instrumentation deployed during MC3E allowed for an integrated analysis of kinematic and microphysical interactions during this event. Figure 11 shows one example of the detailed observations available for storm dynamics studies. In Fig. 11, radar data were gridded using Cressman weighting to 500-m spacing and multi-Doppler synthesis was performed using the National Center for Atmospheric Research's (NCAR) Custom Editing and Display of Reduced Information in Cartesian Space

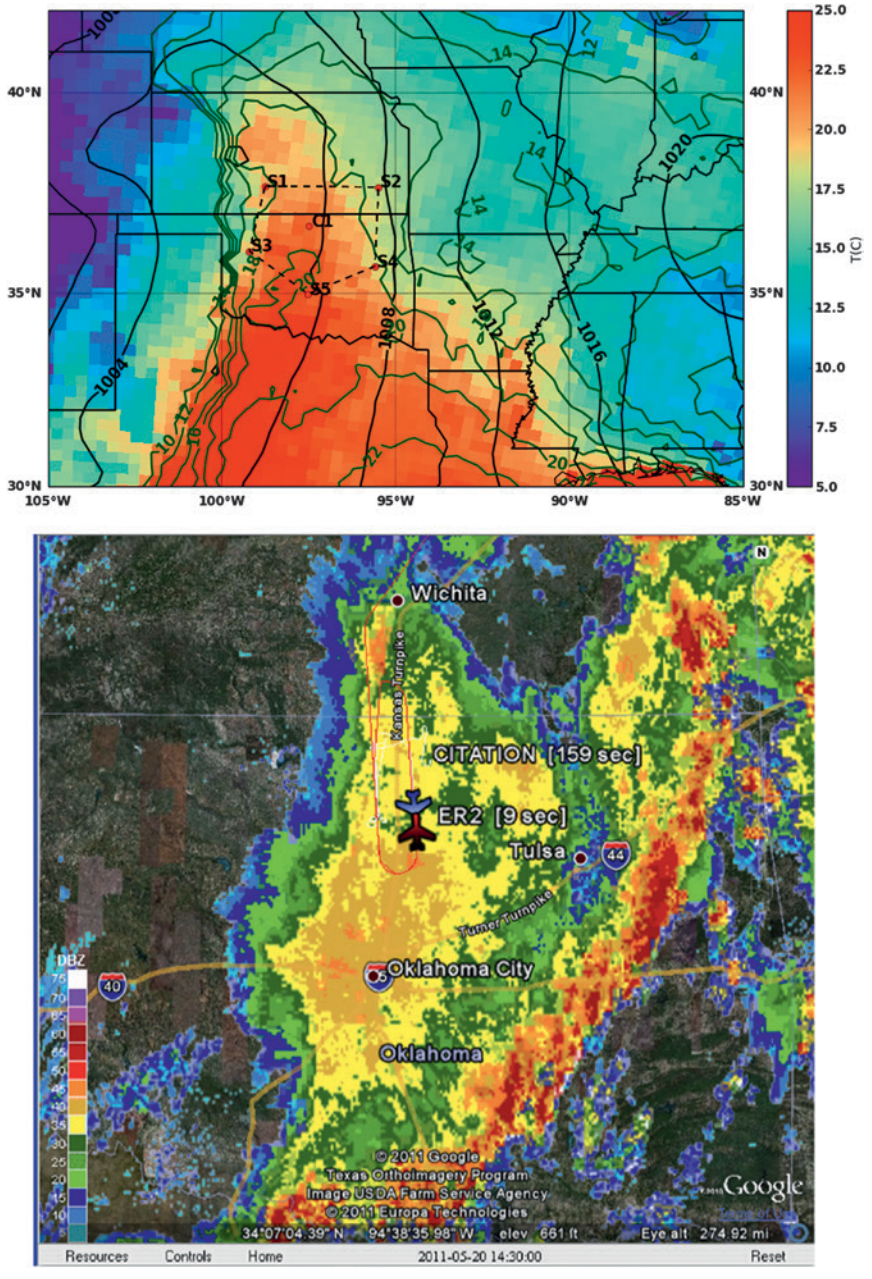

Fig. 8. (top) The 0600 UTC 20 May 2011 surface meteorological analysis based on NARR output showing the surface pressure (hPa; contours) and surface temperature (colors). The MC3E sounding array hexagon is indicated by the dashed lines. (bottom) RTMM image during MC3E field operations showing a PPI of radar reflectivity from the KVNX radar at 1430 UTC with flight positions of ER-2 (red line) and Citation (white line) overlaid in the observational network.

(CEDRIC) analysis package (Mohr and Miller 1983). The multi-Doppler synthesis includes two X-SAPRs and C-SAPR, supplemented with observations from the nearby KVNX radar that provided larger spatial coverage of the storm. The wind field retrievals were derived using variational methods that assume mass continuity (e.g., O'Brien 1970; Ray et al. 1980; Nelson and Brown 1987), techniques that may be further refined using datasets such as those collected during MC3E. High-resolution C-SAPR RHIs (Fig. 11a) showed a deep core extending up to 15 km with an overshooting top, while hydrometeor identification (HID; Dolan et al. 2013; see Fig. 11b) reveals ample hail in the core and melting hail/big drops falling out to the surface beneath the convection (e.g., Gatlin et al. 2015). The multi-Doppler wind analysis matched nearest in time to this detailed RHI indicated a maximum updraft speed exceeding 25 m s^{-1}. Upward motion is also indicated ahead of the main core (~30 km from C-SAPR), perhaps indicating a region of new growth as the storm propagated toward the east-northeast. Lightning analysis from the Oklahoma Lightning Mapping Array (LMA; MacGorman et al. 2008) detected a concentration of flashes on the northern flank of the main updraft (~40 km from C-SAPR), as well as flashes extending into the neighboring stratiform region with the hydrometeor identification suggesting the presence of vertically oriented ice crystals.

Measurements from the UND Citation provided opportunities to evaluate radar retrievals. Figures 12a–d present gridded C-SAPR horizontal (5 km AGL) and vertical slices of equivalent radar reflectivity and HID. During this event, the Citation sampled in rain [as indicated by the high liquid and total water contents near 2133 (~21.55) UTC in Fig. 12e] below a strong convective cell containing hail aloft (according to the hydrometeor

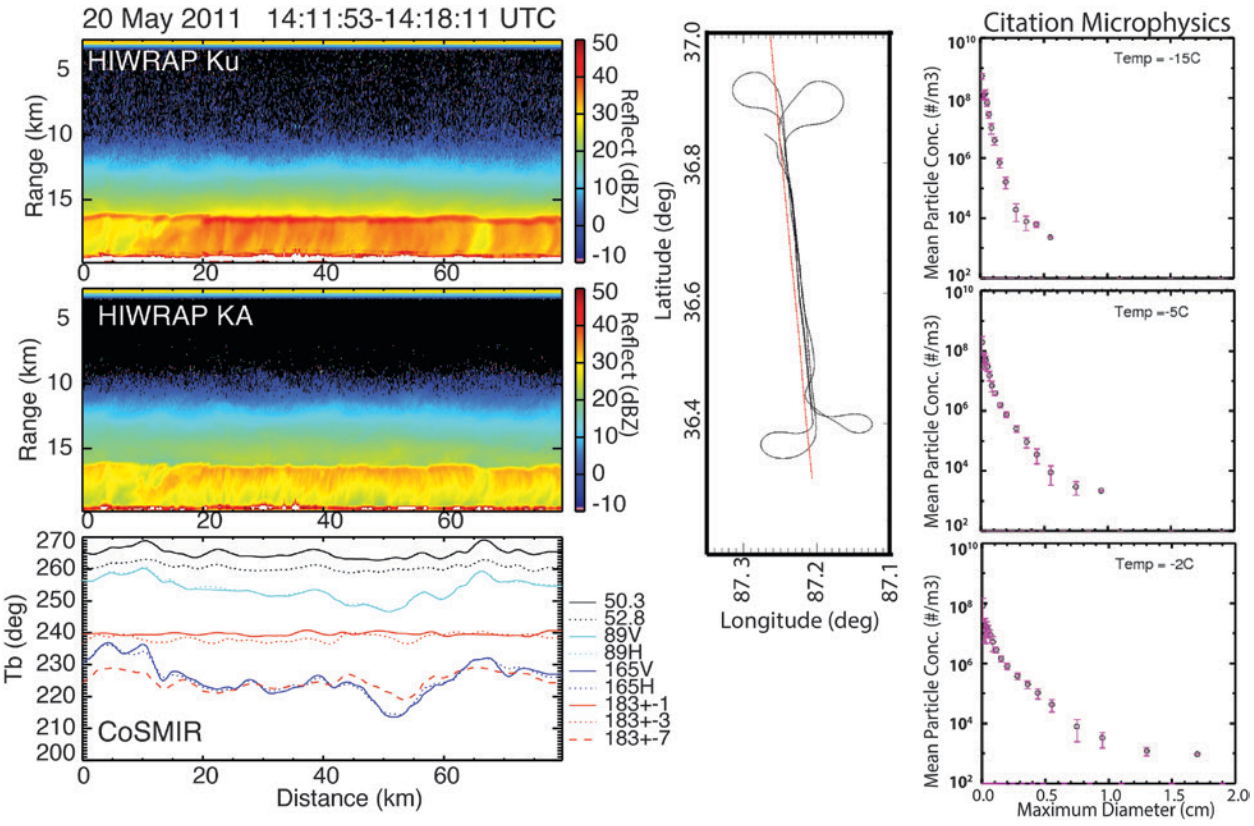

Fig. 9. One flight line from 20 May 2011 during MC3E. (left) Observed reflectivity at (top) Ku and (middle) Ka bands from HIWRAP, and (bottom) CoSMIR brightness temperature. (center) ER2 (red) and Citation (black) flight tracks. (right) Selected PSDs from particle probes on the Citation in the region just above the melting level. The mean particle concentration (blue circle) and error bars (red) for given size bins are shown. The curvature of the plots illustrates the nonexponential behavior of the PSD. The effect of aggregation of small particles as they fall is obvious from the increase in particle size with warmer temperatures.

identification retrieval in Fig. 12d). The Citation then climbed to the south, ascending through ice particles in the anvil to nearly 8 km AGL. The corresponding HID varied between vertical ice and dry snow. In situ measurements aboard the Citation indicated that when sampling in high number concentrations after 2139 (~21.65) UTC, there were particles as large as 1 cm in maximum diameter according to the imaging probe (Fig. 12f; see representative particle image showing snow aggregates at 2140 UTC). One exception was during periods of elevated liquid water, as indicated by the King probe, where decreases in maximum diameter were noted (Fig. 12e). The ice sampled during this ascent tended to increase in bulk density to a value near 0.2 g cm^{-3} [determined via the methodology of Heymsfield et al. (2004) using the particle image shadow areas and the Nevzorov total water content]. This indicated higher-density particles than snow (e.g., Rutledge and Hobbs 1983), consistent with the sampling of rapid mixed-phase growth of ice of convective origin.

PRELIMINARY STUDIES OF RAINFALL AND DSD VARIABILITY. An important goal during MC3E was to quantify the variability of precipitation processes over spatial scales of the GPM core-satellite footprint and smaller to evaluate the impact of subgrid variability on satellite retrievals and model simulations. Seven 2DVDs were positioned within 6 km of the ARM SGP (Fig. 1c), with the maximum and minimum distances between these devices set at 9.2 and 0.35 km, respectively. This maximum distance between the 2DVDs was one way to judge the upper bound for our ability to determine spatial precipitation variability with these systems during MC3E (e.g., Bringi et al. 2015). Approximately six hundred 1-min rainy samples were collected from the 2DVDs, avoiding time periods that may have included hail or mixed precipitation.

Initial 2DVD spatial rainfall variability studies adopted a three-parameter exponential function to represent the degree of horizontal rainfall and DSD parameter variability. A nugget parameter, defined

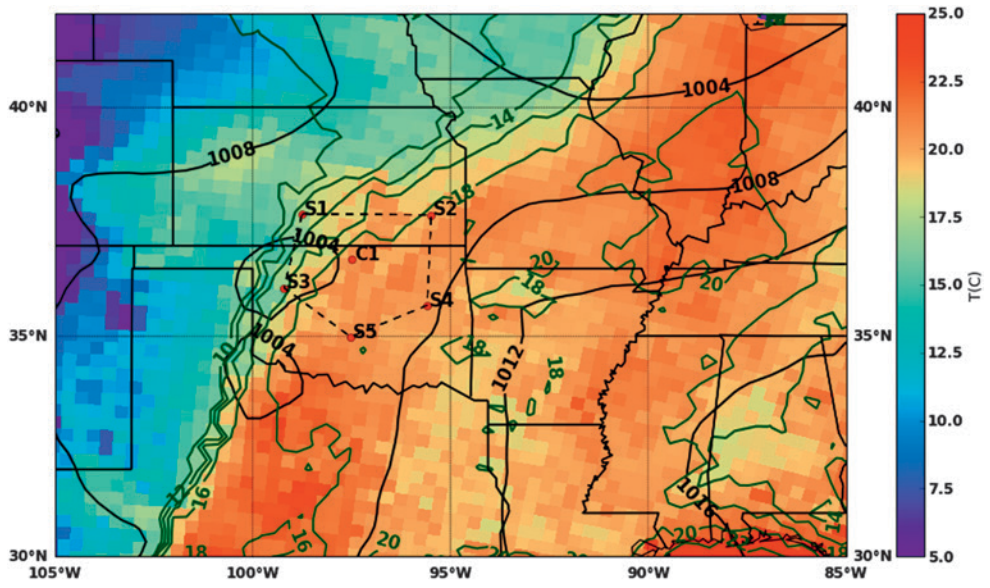

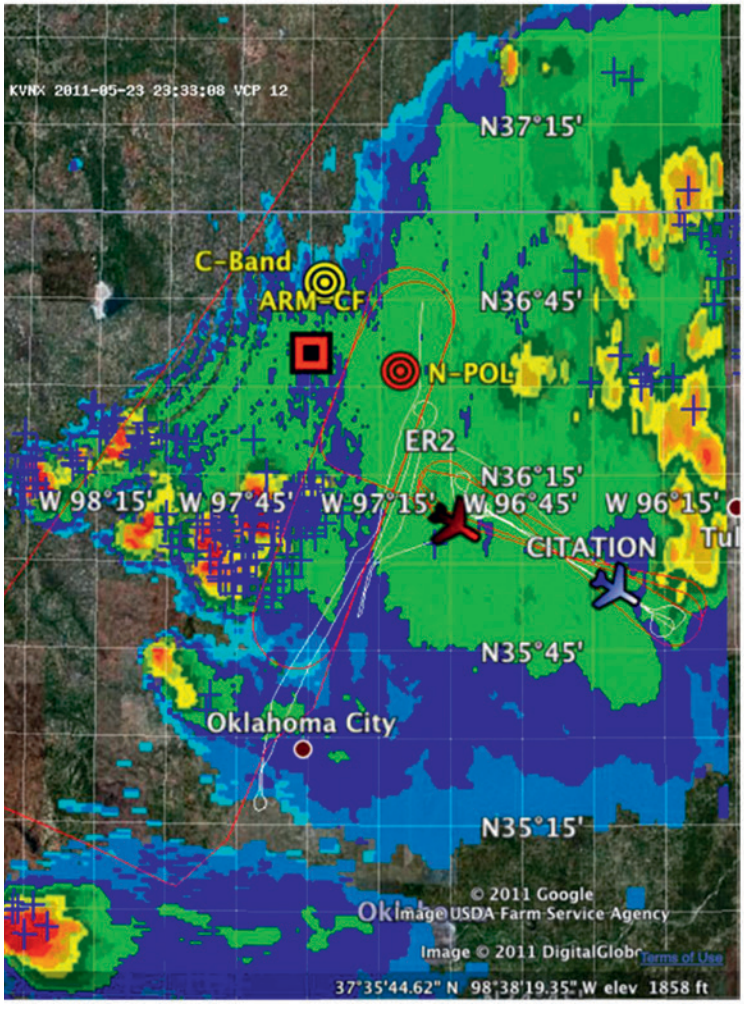

◂ **Fig. 10. (top) The 1200 UTC 23 May 2011 surface meteorological analysis based on NARR output showing the surface pressure (hPa; contours) and surface temperature (colors). The MC3E sounding array hexagon is indicated by the dashed lines. (bottom) RTMM image during MC3E field operations showing a PPI of radar reflectivity from the KVNX radar at 2333 UTC with flight positions of ER-2 (red line) and Citation (white line) overlaid in the observational network. The black/red square is the ARM Central Facility, the yellow bullseye is the C-band radar (C-SAPR), and the red bullseye is the N-Pol.**

▸ **Fig. 11. C-SAPR (a) reflectivity and (b) HID from an RHI at 2229 UTC along a 189° azimuth. Corresponding (c) C-SAPR reflectivity and (d) HID from a PPI at 1.2° at 2230 UTC. Vectors are storm-relative winds resulting from a multiple-Doppler synthesis from C-SAPR, two X-SAPRs, and KVNX at 2223 UTC. Circles denote lightning flashes that originated along the RHI during a 5-min period from 2225 to 2230 UTC, where relative circle size represents the relative flash length. The HID color bar key in (b) and (d) is as follows: UC is unclassified, DZ is drizzle, RN is rain, CR is ice crystals, DS is dry snow, WS is wet snow, VI is vertical ice, LDG is low-density graupel, HDG is high-density graupel, HA is hail, and BD/MH is big drops/melting hail. The light purple polygons in (c) and (d) represent the locations of the RHI.**

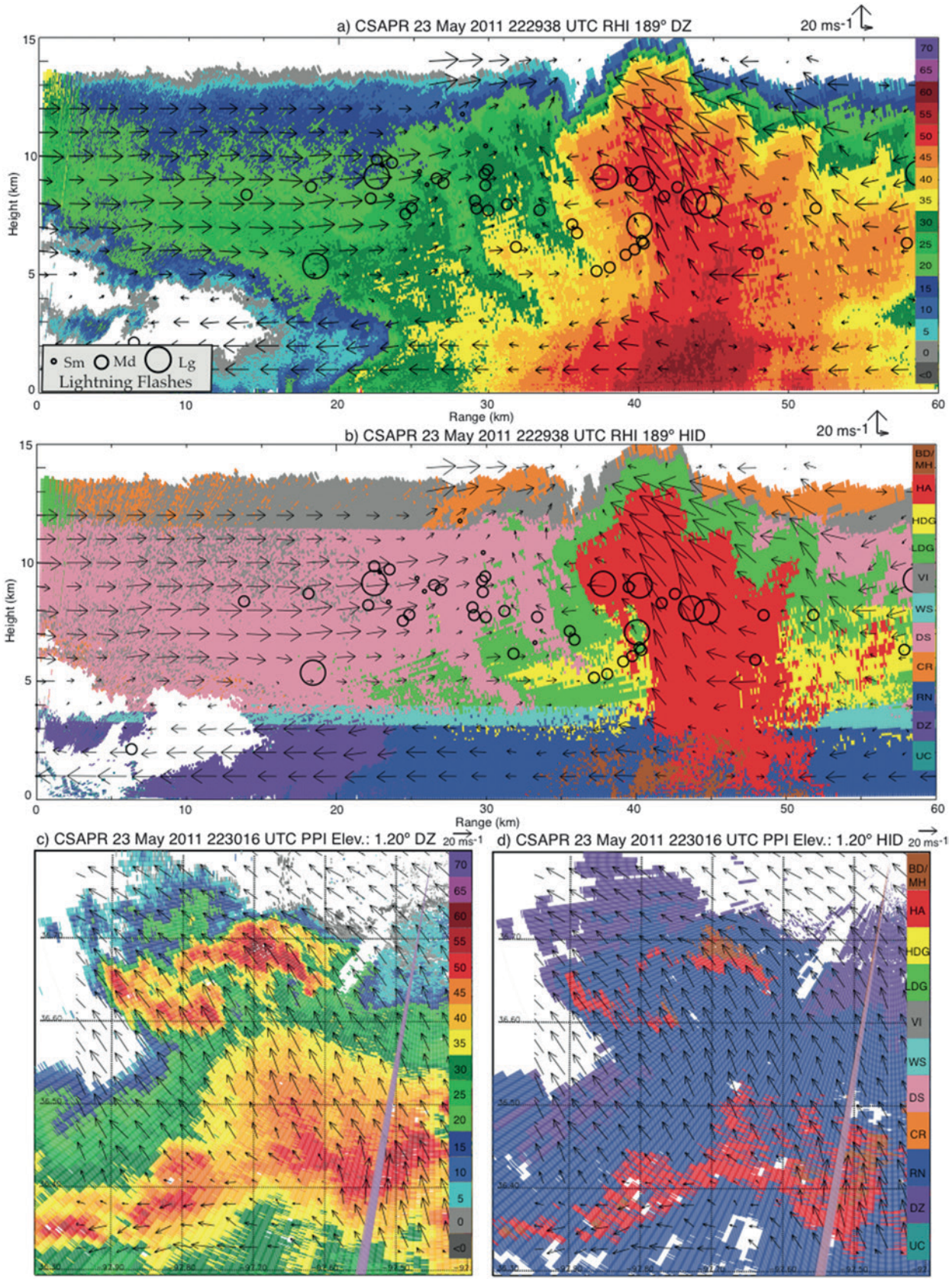
a) CSAPR 23 May 2011 222938 UTC RHI 189° DZ
20 ms-1
Height (km)
Range (km)
Sm Md Lg
Lightning Flashes
b) CSAPR 23 May 2011 222938 UTC RHI 189° HID
20 ms-1
BD/MH
HA
HDG
LDG
VI
WS
DS
CR
RN
DZ
UC
c) CSAPR 23 May 2011 223016 UTC PPI Elev.: 1.20° DZ
20 ms-1
d) CSAPR 23 May 2011 223016 UTC PPI Elev.: 1.20° HID
20 ms-1

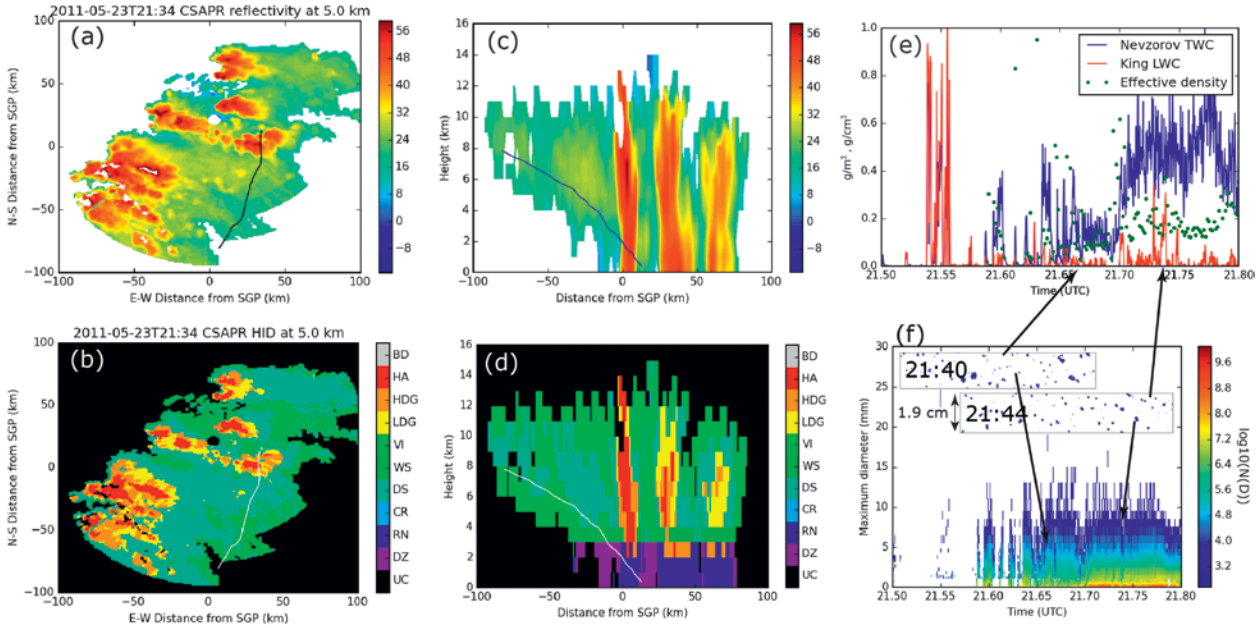

Fig. 12. For the C-SAPR at 2134 UTC 23 May 2011, the (a) gridded effective reflectivity factor at 5 km AGL, (b) Colorado State University (CSU) hydrometeor identification, (c) at x = 25 km, a vertical cross section of the effective reflectivity factor, and (d) at x = 25 km, a vertical cross section of CSU hydrometeor identification. The track of the UND Citation aircraft from 2130 to 2148 UTC is shown with a black line in (a) and (c) and a white line in (b) and (d). (e) Over the same time period, a time series of the Nevzorov probe total water content (blue; g m^{-3}), King probe liquid water content (red; g m^{-3}), and effective density (dots; g m^{-3}). (f) A time series of the combined HVPS-3 probe and the CIP PSDs (shaded; log scale). The insets show HVPS-3 probe imagery from two selected times: 2140 and 2144 UTC. The scale of the HVPS-3 image is shown.

as the correlation between rainfall distribution parameters from collocated 2DVD instruments, was also considered and this instrument correlation was allowed to vary between 0.90 and 0.99 (Tokay and Ozturk 2012; Tokay et al. 2014). A correlation distance may then be extracted from this dataset by minimizing the RMSE between the observed and predicted correction at a given distance. For warm-season precipitation in northern Oklahoma, a finding of a 4-km correlation distance for rainfall fits well with the expectation for convective cells (Fig. 13a). The observed correlations mostly followed the fitted curve, having an rmse of 0.12. The mass-weighted drop diameter D_m displayed an excellent fit, with an rmse less than 0.06 for the MC3E events. The correlation distance for D_m ranged from 5.0 to 5.5 km, depending on the nugget parameter (Fig. 13b).

CONCLUSIONS AND FUTURE DIRECTIONS. NASA and DOE collaborated in MC3E to collect measurements characterizing the four-dimensional properties of convective clouds and precipitation for the purposes of improving the representation of the convective life cycle in atmospheric models and the reliability of satellite-based retrievals of precipitation. Toward these goals, three major targets of the campaign were 1) observations of the vertical and horizontal structure of the atmospheric thermodynamic state for the derivation of large-scale forcing conditions for cloud-model simulations, 2) characterization of the variability of cloud and precipitation microphysical properties through the convective cloud life cycle, and 3) identification of updraft and downdraft dynamics within convective clouds. Through discussion of three precipitation events observed during MC3E, the manuscript presents examples of how these targets were achieved with examples of analyses from the major observational platforms. The coordinated efforts resulted in a very successful MC3E field campaign whose datasets will be the focus of scientific research for many years. Ongoing and future research efforts are aimed at using these observations to find new insights into the dynamics and microphysics of deep convective systems that will lead to improvements in model simulations and retrievals.

There are a number of current and ongoing research projects using the MC3E dataset. A few of the recently completed, current, and anticipated research activities are related to the numerical modeling of

continental precipitating systems (e.g., Tao et al. 2013; Gustafson et al. 2014; Lang et al. 2014), satellite-based precipitation retrieval algorithm development and associated ground validation studies (e.g., Matsui et al. 2013; Heymsfield et al. 2013; Kuo et al. 2016; Olson et al. 2016; Bringi et al. 2015; Leppert and Cecil 2015; Williams 2016), deep convective vertical velocities (Giangrande et al. 2013a), the tracking and large-eddy simulation (LES)-scale modeling of shallow cumulus (Borque et al. 2014; Mechem et al. 2015), dual-polarization radar rainfall processing and estimation at shorter wavelengths (Giangrande et al. 2013b; Giangrande et al. 2014), evaluation of reanalysis product representation of the low-level jet (Berg et al. 2015), and studies of cold pools and convective redevelopment, melting-layer precipitation microphysics studies (Heymsfield et al. 2015).

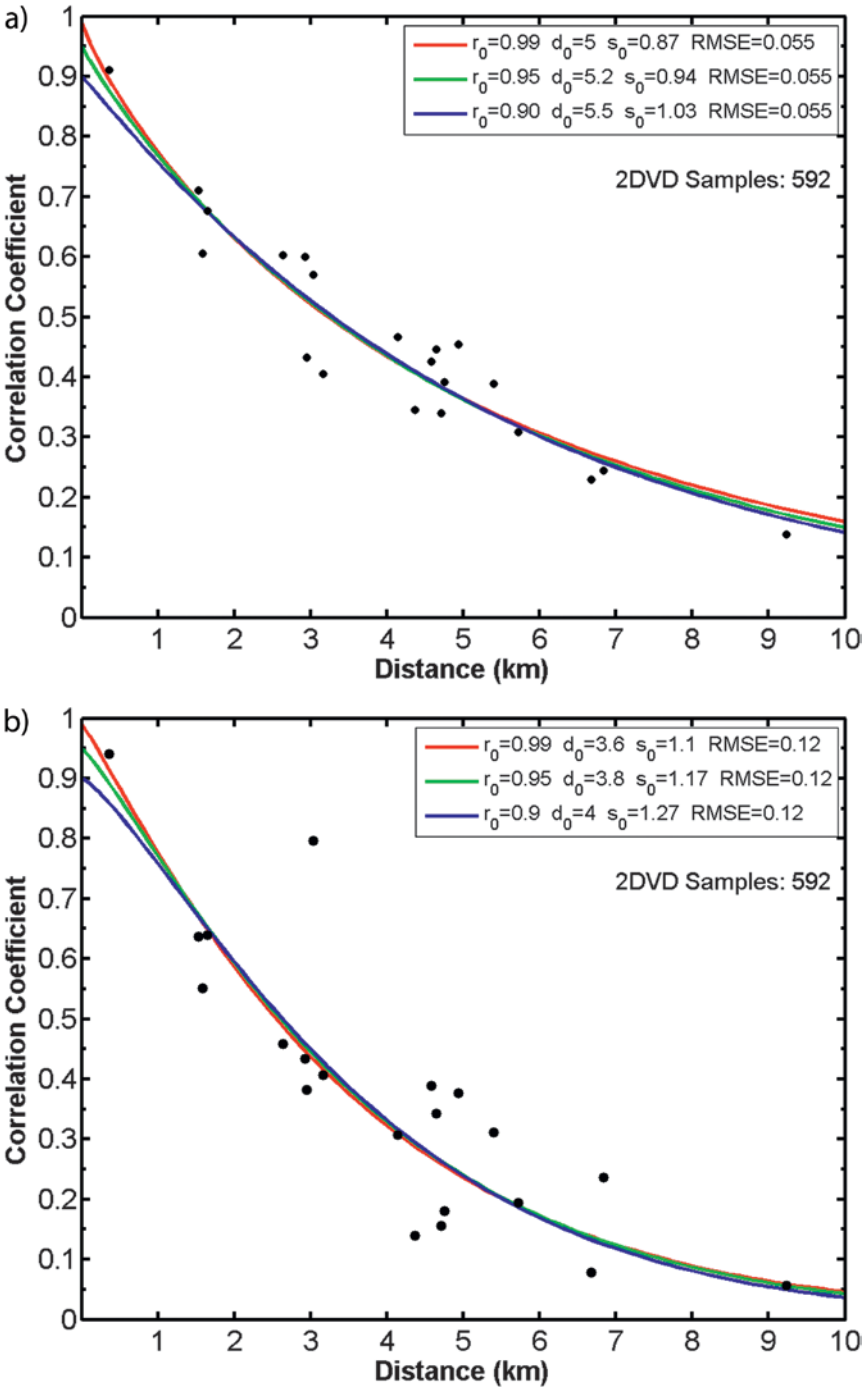

Fig. 13. Correlation coefficient (correlations between collocated 2DVD instruments) as a function of distance for warm-season MC3E precipitation events. These correlations are plotted for the estimates of (a) rainfall and (b) the mass-weighted drop diameter.

ACKNOWLEDGMENTS.
The MC3E field campaign was jointly funded by the U.S. Department of Energy's ARM Program and NASA's Global Precipitation Measurement mission's Ground Validation Program. We acknowledge the important contributions of the ARM SGP site operations staff members for their contributions to the siting, deployment, and maintenance of NASA MC3E and SGP ARM Climate Facility instrumentation. We also acknowledge the UND Citation flight and support crews for their excellent conduct of airborne microphysical sampling, and Offutt AFB and Ponca City Regional Airport for their hosting and field support of the NASA ER-2 and UND Citation, respectively. Operations of the UND Citation aircraft were funded under NASA Grant NNX10AN38G. MJ and SG were funded by the U.S. Department of Energy, Office of Science, Office of Biological and Environmental Research (BER), as part of the Atmospheric System Research (ASR) and ARM programs. AH and AB were funded by NASA Grant NNX10AH67G. SR and BD were

funded by DOE Grant DE-SC0007016 and NASA Grant NNX14AH06G. This paper has been coauthored by employees of Brookhaven Science Associates, LLC, under Contract DE-AC02-98CH10886 with the U.S. Department of Energy.

APPENDIX: MC3E DATASET ACCESS.

Following DOE and NASA data-sharing policies, all data collected during MC3E is publicly available. Data are stored in several different archives depending on the funding agency, measurement status, and data product type. NASA-funded measurements including those from the ER-2 and Citation platforms, the N-POL and disdrometer, and the rain gauge network are archive by the Global Hydrology Resource Center (GHRC) on the GPM Ground Validation Data portal (http://gpm.nsstc.nasa.gov/). All standard ARM observations at the SGP including radar, lidar, radiation, and meteorology are available via the ARM data archive (www.archive.arm.gov). Campaign-specific datasets collected during MC3E under ARM funding are available in the ARM Intensive Operational Period (IOP) archive (http://iop.archive.arm.gov/arm-iop/2011/sgp/mc3e).

REFERENCES

Ackerman, T. P., and G. M. Stokes, 2003: The Atmospheric Radiation Measurement Program. *Phys. Today*, **56**, 38–45, doi:10.1063/1.1554135.

Berg, L. K., L. D. Riihimaki, Y. Qian, H. Yan, and M. Huang, 2015: The low-level jet over the southern Great Plains determined from observations and reanalyses and its impact on moisture transport. *J. Climate*, **28**, 6682–6706, doi:10.1175/JCLI-D-14-00719.1.

Blakeslee, R., J. Hall, M. Goodman, P. Parker, L. Freudinger, and M. He, 2007: The NASA Real Time Mission Monitor—A situational awareness tool for managing experiment assets. P*roc. NASA Science and Technology Conf. 2007*, College Park, MD, NASA, A3P2. [Available online at http://rtmm.nsstc.nasa.gov/documents/nstc2007_rtmm_a3p2.pdf.]

Borque, P., P. Kollias, and S. Giangrande, 2014: First observations of tracking clouds using scanning ARM cloud radars. *J. Appl. Meteor. Climatol.*, **53**, 2732–2746, doi:10.1175/JAMC-D-13-0182.1.

Bringi, V. N., L. Tolstoy, M. Thurai, and W. A. Petersen, 2015: Estimation of spatial correlation of rain drop size distribution parameters and rain rate using NASA's S-band polarimetric radar and 2D-video disdrometer network: Two case studies from MC3E. *J. Hydrometeor.*, **16**, 1207–1221, doi:10.1175/JHM-D-14-0204.1.

Dolan, B., S. A. Rutledge, S. Lim, V. Chandrasekar, and M. Thurai, 2013: A robust C-band hydrometeor identification algorithm and application to a long-term polarimetric radar dataset. *J. Appl. Meteor. Climatol.*, **52**, 2162–2186, doi:10.1175/JAMC-D-12-0275.1.

Gatlin, P., M. Thurai, V. N. Bringi, W. Petersen, D. B. Wolff, A. Tokay, L. D. Carey, and M. Wingo, 2015: Searching for large raindrops: A global summary of two-dimensional video disdrometer observations. *J. Appl. Meteor. Climatol.*, **54**, 1069–1089, doi:10.1175/JAMC-D-14-0089.1.

Gerlach, J., and W. A. Petersen, 2011: NPOL: The NASA transportable S-band dual-polarimetric radar. Antenna system upgrades, performance and deployment during MC3E. *Proc. 35th Conf. on Radar Meteorology*, Pittsburgh, PA, Amer. Meteor. Soc., 192. [Available online at https://ams.confex.com/ams/35Radar/webprogram/Paper191918.html.]

Giangrande, S. E., S. Collis, J. Straka, A. Protat, C. Wiliams, and S. Krueger, 2013a: A summary of convective-core vertical velocity properties using ARM UHF wind profilers in Oklahoma. *J. Appl. Meteor. Climatol.*, **52**, 2278–2295, doi:10.1175/JAMC-D-12-0185.1.

——, R. McGraw, and L. Lei, 2013b: An application of linear programming to polarimetric radar differential phase processing. *J. Atmos. Oceanic Technol.*, **30**, 1716–1729, doi:10.1175/JTECH-D-12-00147.1.

——, S. Collis, A. K. Theisen, and A. Tokay, 2014: Precipitation estimation from the ARM distributed radar network during the MC3E campaign. *J. Appl. Meteor. Climatol.*, **53**, 2130–2147, doi:10.1175/JAMC-D-13-0321.1.

Gustafson, W. I., Jr., P.-L. Ma, and B. Singh, 2014: Precipitation microphysics of CAM5 physics at mesoscale resolution during MC3E and the impact of convective timescale choice. *J. Adv. Model. Earth Syst.*, **6**, 1271–1287, doi:10.1002/2014MS000334.

Heistermann, M., and Coauthors, 2015: The emergence of open source software for the weather radar community. *Bull. Amer. Meteor. Soc.*, **96**, 117–128, doi:10.1175/BAMS-D-13-00240.1.

Heymsfield, A. J., C. G. Schmitt, A. Bansemer, D. Baumgardner, E. M. Weinstock, J. T. Smith, and D. Sayres, 2004: Effective ice particle densities for cold anvil cirrus. *Geophys. Res. Lett.*, **31**, L02101, doi:10.1029/2003GL018311.

——, A. Bansemer, M. R. Poellot, and N. Wood, 2015: Observations of ice microphysics through the melting layer. *J. Atmos. Sci.*, **72**, 2902–2928, doi:10.1175/JAS-D-14-0363.1.

Heymsfield, G. M., L. Tian, L. Li, M. McLinden, and J. I. Cervantes, 2013: Airborne radar observations

of severe hailstorms: Implications for future spaceborne radar. *J. Appl. Meteor. Climatol.*, **52**, 1851–1867, doi:10.1175/JAMC-D-12-0144.1.

Hou, A. Y., and Coauthors, 2014: The Global Precipitation Measurement Mission. *Bull. Amer. Meteor. Soc.*, **95**, 701–722, doi:10.1175/BAMS-D-13-00164.1.

Houze, R., Jr., 2014: *Cloud Dynamics.* Academic Press. 496 pp.

Jensen, M. P., and Coauthors, 2010: Mid-Latitude Continental Convective Cloud Experiment (MC3E) science and implementation plan. DOE/ARM Tech. Rep. DOE/SC-ARM/10-004, 31 pp. [Available online at www.arm.gov/publications/programdocs/doe-sc-arm-10-004.pdf.]

——, T. Toto, D. Troyan, D. Holdridge, J. Kyrouac, and J. Schatz, 2015: The MC3E sounding network: Operations, processing and analysis. *Atmos. Meas. Tech.*, **8**, 421–434, doi:10.5194/amt-8-421-2015.

Klein, S. A., and A. D. Del Genio, 2006: ARM's support for GCM improvement: A white paper. DOE/SC-ARM/P-06-012, U.S. Department of Energy, 12 pp. [Available online at www.arm.gov/publications/programdocs/doe-sc-arm-0612.pdf.]

Kollias, P., M. A. Miller, E. P. Luke, K. L. Johnson, E. E. Clothiaux, K. P. Moran, K. B. Widener, and B. A. Albrecht, 2007: The Atmospheric Radiation Measurement program cloud profiling radars: Second-generation sampling strategies, processing, and cloud data products. *J. Atmos. Oceanic Technol.*, **24**, 1199–1214, doi:10.1175/JTECH2033.1.

——, N. Bharadwaj, K. Widener, I. Jo, and K. L. Johnson, 2014a: Scanning ARM cloud radars: Part I: Operational sampling strategies. *J. Atmos. Oceanic Technol.*, **31**, 569–582, doi:10.1175/JTECH-D-13-00044.1.

——, I. Jo, P. Borque, A. Tatarevic, K. Lamer, N. Bharadwaj, K. Widener, K. L. Johnson, and E. E. Clothiaux, 2014b: Scanning ARM cloud radars. Part II: Data quality control and processing. *J. Atmos. Oceanic Technol.*, **31**, 583–598, doi:10.1175/JTECH-D-13-00045.1.

Kuo, K.-S., W. S. Olson, and B. T. Johnson, 2016: The microwave radiative properties of falling snow derived from nonspherical ice particle models. Part I: An extensive database of simulated pristine crystals and aggregate particles, and their scattering properties. *J. Appl. Meteor. Climatol.*, **55**, 691–708, doi:10.1175/JAMC-D-15-0130.1.

Lang, S., W. Tao, J. Chern, D. Wu, and X. Li, 2014: Benefits of a fourth ice class in the simulated radar reflectivities of convective systems using a bulk microphysics scheme. *J. Atmos. Sci.,* **71**, 3583–3612, doi:10.1175/JAS-D-13-0330.1.

Leppert, K. G., II, and D. J. Cecil, 2015: Signatures of hydrometeor species from airborne passive microwave data for frequencies 10–183 GHz. *J. Appl. Meteor. Climatol.*, **54**, 1313–1334, doi:10.1175/JAMC-D-14-0145.1.

Long, C. N., D. W. Slater, and T. Tooman, 2001: Total sky imager model 880 status and testing results. ARM Tech. Rep. ARM TR-006, 17 pp. + appendixes. [Available online at www.arm.gov/publications/tech_reports/arm-tr-006.pdf.]

MacGorman, D. R., and Coauthors, 2008: TELEX: The Thunderstorm Electrification and Lightning Experiment. *Bull. Amer. Meteor. Soc.*, **89**, 997–1013, doi:10.1175/2007BAMS2352.1.

Mather, J. H., and J. W. Voyles, 2013: The ARM Climate Research Facility: A review of structure and capabilities. *Bull. Amer. Meteor. Soc.*, **94**, 377–392, doi:10.1175/BAMS-D-11-00218.1.

Matsui, T. T., and Coauthors, 2013: GPM satellite simulator over ground validation sites. *Bull. Amer. Meteor. Soc.*, **94**, 1653–1660, doi:10.1175/BAMS-D-12-00160.1.

Mechem, D. B., S. E. Giangrande, C. S. Wittman, P. Borque, T. Toto, and P. Kollias, 2015: Insights from modeling and observational evaluation of a precipitating continental cumulus event observed during the MC3E field campaign. *J. Geophys. Res. Atmos.*, **120**, 1980–1995, doi:10.1002/2014JD022255.

Mohr, C. G., and L. J. Miller, 1983: CEDRIC—A software package for Cartesian space editing, synthesis and display of radar fields under interactive control. Preprints, *21st Conf. on Radar Meteorology*, Edmonton, AB, Canada, Amer. Meteor. Soc., 569–574.

Nelson, S. P., and R. A. Brown, 1987: Error sources and accuracy of vertical velocities computed from multiple-Doppler radar measurements in deep convective storms. *J. Atmos. Oceanic Technol.*, **4**, 233–238, doi:10.1175/1520-0426(1987)004<0233:ESAAOV>2.0.CO;2.

O'Brien, J. J., 1970: Alternative solutions to the classical vertical velocity problem. *J. Appl. Meteor.*, **9**, 197–203, doi:10.1175/1520-0450(1970)009<0197:ASTTCV>2.0.CO;2.

Olson, W. S., K.-S. Kuo, L. Tian, M. Grecu, B. T. Johnson, A. J. Heymsfield, and G. M. Heymsfield, 2016: The microwave radiative properties of falling snow derived from nonspherical ice particle models. Part II: Initial testing using radar, radiometer, and in situ observations. *J. Appl. Meteor. Climatol.*, **55**, 709–722 doi:10.1175/JAMC-D-15-0131.1.

Petersen, W. A., and M. P. Jensen, 2012: The NASA-GPM and DOE-ARM Midlatitude Continental Convective Clouds Experiment (MC3E). *Int. J. Appl. Earth Obs.*, **24**, 12–18.

Ray, P. S., C. L. Ziegler, W. Bumgarner, and R. J. Serafin, 1980: Single- and multiple-Doppler radar

observations of tornadic storms. *Mon. Wea. Rev.*, **108**, 1607–1625, doi:10.1175/1520-0493(1980)108<1607:SAMDRO>2.0.CO;2.

Rutledge, S. A., and P. V. Hobbs, 1983: The mesoscale and microscale structure and organization of clouds and precipitation in midlatitude cyclones. VIII: A model for the "seeder-feeder" process in warm-frontal rainbands. *J. Atmos. Sci.*, **40**, 1185–1206, doi:10.1175/1520-0469(1983)040<1185:TMAMSA>2.0.CO;2.

Saavedra, P., A. Battaglia, and C. Simmer, 2011: Partitioning of cloud water and rain water content by ground-based observations with the Advanced Microwave Radiometer for Rain Identification (ADMIRARI) in synergy with a Micro Rain Radar. *J. Geophys. Res.*, **117**, D05203, doi:10.1029/2011JD016579.

Schönhuber, M., G. Lammer, and W. L. Randeu, 2008: The 2D video distrometer. *Precipitation: Advances in Measurement, Estimation and Prediction*, S. Michaelides, Ed., Springer, 3–31.

Spencer, R. W., R. E. Hood, F. J. LaFontaine, E. A. Smith, R. Platt, J. Galliano, V. L. Griffin, and E. Lobl, 1994: High-resolution imaging of rain systems with the Advanced Microwave Precipitation Radiometer. *J. Atmos. Oceanic Technol.*, **11**, 849–857, doi:10.1175/1520-0426(1994)011<0849:HRIORS>2.0.CO;2.

Stokes, G. M., and S. E. Schwartz, 1994: The Atmospheric Radiation Measurement (ARM) program: Programmatic background and design of the Cloud and Radiation Test Bed. *Bull. Amer. Meteor. Soc.*, **75**, 1201–1221, doi:10.1175/1520-0477(1994)075<1201:TARMPP>2.0.CO;2.

Tao, W. K., and Coauthors, 2013: Precipitation intensity and variation during MC3E: A numerical modeling study. *J. Geophys. Res. Atmos.*, **118**, 7199–7218, doi:10.1002/jgrd.50410.

Thurai, M., W. A. Petersen, A. Tokay, C. Schultz, and P. Gatlin, 2011: Drop size distribution comparisons between Parsivel and 2D video disdrometers. *Adv. Geosci.*, **30**, 3–9, doi:10.5194/adgeo-30-3-2011.

Tokay, A., and K. Ozturk, 2012: An experimental study of the small-scale variability of rainfall. *J. Hydrometeor.*, **13**, 351–365, doi:10.1175/JHM-D-11-014.1.

——, W. A. Petersen, P. Gatlin, and M. Wingo, 2013: Comparison of raindrop size distribution measurements by collocated disdrometers. *J. Atmos. Oceanic Technol.*, **30**, 1672–1690, doi:10.1175/JTECH-D-12-00163.1.

——, R. J. Roche, and P. G. Bashor, 2014: An experimental study of spatial variability of rainfall. *J. Hydrometeor.*, **15**, 801–812, doi:10.1175/JHM-D-13-031.1.

Tridon, F., A. Bataglia, P. Kollias, E. P. Luke, and C. R. Williams, 2013: Signal processing and reflectivity calibration of the Atmospheric Radiation Measurement program 915-MHz wind profilers. *J. Atmos. Oceanic Technol.*, **30**, 1038–1054, doi:10.1175/JTECH-D-12-00146.1.

Vega, M., J. Carswell, V. Chandrasekar, M. Schwaller, and K.V. Mishra, 2010: Realization of the NASA Dual-Frequency Dual-Polarized Doppler Radar (D3R). *Proc. Int. Geosciences and Remote Sensing Symp.*, Honolulu, HI, IEEE, 4815–4818, doi:10.1109/IGARSS.2010.5653929.

——, V. Chandrasekar, J. Carswell, R. M. Beauchamp, M. R. Schwaller, and C. M. Nguyen, 2014: Salient features of the dual-frequency, dual-polarized, Doppler radar for remote sensing of precipitation. *Radio Sci.*, **49**, 1087–1105, doi:10.1002/2014RS005529.

Wang, J. R., P. E. Racette, J. E. Piepmeier, B. Monosmith, and W. Manning, 2007: Airborne CoSMIR observations between 50 and 183 GHz over snow-covered Sierra Mountains. *IEEE Trans. Geosci. Remote Sens.*, **45**, 55–61, doi:10.1109/TGRS.2006.885410.

Williams, C. R., 2012: Vertical air motion retrieved from dual-frequency profiler observations. *J. Atmos. Oceanic Technol.*, **29**, 1471–1480, doi:10.1175/JTECH-D-11-00176.1.

——, 2016: Reflectivity and liquid water content vertical decomposition diagrams to diagnose vertical evolution of raindrop size distributions. *J. Atmos. Oceanic Technol.*, **33**, 579-594. doi:10.1175/JTECH-D-15-0208.1.

Xie, S., Y. Zhang, S. E. Giangrande, M. P. Jensen, R. McCoy, and M. Zhang, 2014: Interactions between cumulus convection and its environment as revealed by the MC3E sounding array. *J. Geophys. Res. Atmos.*, **119**, 11 784–11 808, doi:10.1002/2014JD022011.

Zhang, M. H., and J. L. Lin, 1997: Constrained variational analysis of sounding data based on column-integrated budgets of mass, heat, moisture, and momentum: Approach and application to ARM measurements. *J. Atmos. Sci.*, **54**, 1503–1524, doi:10.1175/1520-0469(1997)054<1503:CVAOSD>2.0.CO;2.